Available online at www.sciencedirect.com
ScienceDirect
Journal of Nuclear Materials 371 (2007) 304–313
journal of nuclear materials
www.elsevier.com/locate/jnucmat

Shear properties at the PyC/SiC interface of a TRISO-coating

T. Nozawa *, L.L. Snead, Y. Katoh, J.H. Miller

Materials Science and Technology Division, Oak Ridge National Laboratory, P.O. Box 2008, 1 Bethel Valley Road, Oak Ridge, TN 37831-6138, USA

Abstract

The failure behavior of TRISO-coated fuel particles depends significantly on the shear strength at the interface between the inner pyrolytic carbon (PyC) and silicon carbide (SiC) coatings. In this study, a micro-indentation fiber push-out test was applied to measure the interfacial shear properties of a model TRISO-coated tube. Of particular emphasis is that this study developed a non-linear shear-lag model for a transversely isotropic composite material due to insufficiency in the existing isotropic models as applied to layered TRISO-coating systems. In the model, the effects of thermal residual stresses and the roughness-induced clamping stress were identified as particularly important. The rigorous model proposed in this study provides more reasonable data on two important interfacial parameters: the interfacial debond shear strength and the interfacial friction stress. The modified model coupled with experiments yields an interfacial debond shear strength of 240 ± 40 MPa. This high interfacial strength, though slightly lower than that obtained by the existing isotropic model ($\sim$280 MPa), allows significant loads to be transferred between inner PyC and SiC in application. Additionally, an interfacial friction stress of 120 ± 30 MPa was determined. This high friction stress is attributed primarily to the roughness at the cracked interface rather than clamping effects due to differing coefficients of thermal expansion.
Published by Elsevier B.V.

1. Introduction

A TRISO-coated nuclear fuel system is one of the advanced fuel concepts for the very high temperature gas-cooled test reactor (VHTR) [1]. The TRISO-coated fuel particle is composed of a fissionable kernel core and four functional overlayers: a low-density buffer pyrolytic carbon (BPyC) layer, a dense inner pyrolytic carbon (IPyC) layer, a silicon carbide (SiC) layer, and a dense outer pyrolytic carbon (OPyC) layer. In this fuel system, the SiC coating layer is essentially impervious to fission gases at normal operating temperatures and primarily acts as a structural material. To achieve better fuel performance and enhanced fuel lifetime, a high reliability SiC layer is critical.

For many of the potential failure mechanisms of a TRISO fuel, the load transmitted across the IPyC/SiC interface, along with the strength of the SiC layer itself [2], is of fundamental importance. If the interfacial shear strength is very high, no debonding or partial debonding would occur, leading to a stress concentration in the SiC coating around the crack tip. In contrast, the complete interfacial debonding due to low interfacial strength may cause a pressure vessel type fracture of the SiC coating.

* Corresponding author. Tel.: +1 865 576 6301; fax: +1 865 241 3650.
E-mail address: nozawat@ornl.gov (T. Nozawa).

0022-3115/$ - see front matter Published by Elsevier B.V.
doi:10.1016/j.jnucmat.2007.05.015

Nozawa et al. [3] evaluated the shear properties of the IPyC/SiC interface using a simulated TRISO-coated tubular material. A micro-indentation fiber push-out technique, originally developed to determine the interfacial shear properties of composite materials [4], was applied to evaluate two important parameters: (1) an interfacial debond shear strength, which can initiate a primary crack at the perfectly bonded interface, and (2) an interfacial friction stress at the debonded interface. Assuming that both the inner core, which is composed of kernel, BPyC and IPyC, and the SiC layer are isotropic, the non-linear shear-lag models developed by Hsueh [5] and Shetty [6] were applied to predict the interfacial debond shear strength and the interfacial friction stress, respectively. However the modeled TRISO-coated tube is transversely isotropic. Therefore, further improvement of the analytical models is required to quantify the interfacial shear properties of the TRISO-coating. Additionally, thermal expansion mismatch-induced residual stresses and roughness-induced clamping stress may impact the interfacial shear properties, although they were ignored in the preliminary analysis for simplicity.

This study aims to evaluate the interfacial shear properties of the IPyC/SiC interface in a model TRISO-coated tubular material using the micro-indentation push-out test technique. Specifically, a modified non-linear shear-lag model for a transversely isotropic composite material was developed to evaluate the interfacial shear properties. The effects of thermally-induced residual stresses and roughness-induced clamping stress were considered in the model because of their particular importance.

2. Experimental

2.1. Material

A model TRISO-coated tubular material was fabricated by chemical vapor deposition (CVD). Deposition conditions were the same as those used for actual TRISO fuel preparation [2]. A typical cross-sectional micrograph is shown in Fig. 1. A SCS-9A™ 'SiC' based fiber (Specialty Materials, Inc., Lowell, MA) with a diameter of ~75 μm and a length of ~5 mm was used as a core material. The obvious simplification being made here is to prepare a cylindrical TRISO surrogate which lends itself to mechanical testing as compared to a spherical TRISO fuel. A buffer porous PyC with a thickness of ~40 μm was formed on the surface of

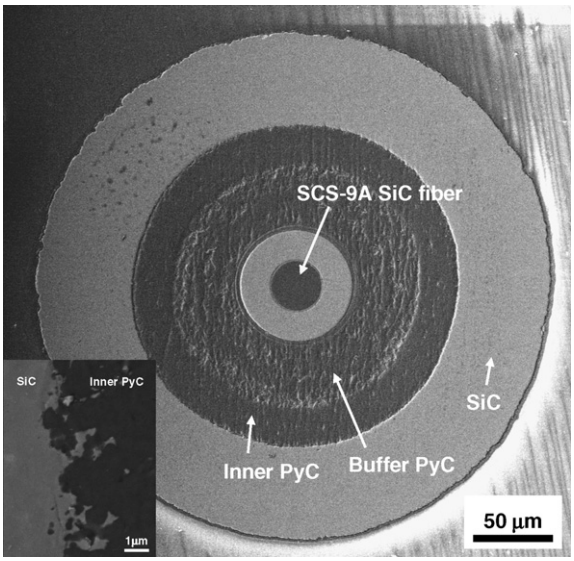

Fig. 1. A typical cross-sectional image of a model TRISO-coated tube.

SCS-9A™ fiber. A ~23 μm-thick inner dense PyC and a ~60 μm-thick SiC were subsequently deposited. No outer PyC coating was formed. The details of the material fabrication were described in the previous work by the authors [3].

2.2. Micro-indentation push-out test

Shear properties of the IPyC/SiC interface were evaluated by the micro-indentation fiber push-out technique [4]. Thinly-sliced specimens, which were polished using standard metallographic techniques to a thickness ranging from 60 to 340 μm, with a surface finish of 1–5 μm, were bonded to a specimen holder above a ~230 μm-diameter hole. The fiber core (a SCS-9A™ fiber with buffer and inner PyC layers) was punched-out with a conical indenter with a flat-bottomed tip. The crosshead displacement rate applied to the fiber core was 20 μm/min. The details of the experimental procedure were described elsewhere [3].

A modified non-linear shear-lag model for a transversely isotropic composite material was applied to evaluate the interfacial debond shear strength and the interfacial friction stress. For simplicity, a two-phase model, considering the stress balance at the interface separated between the pushed-out fiber core (SCS-9A™ + BPyC + IPyC) and the SiC coating, was developed. Details of the models are described in the following section.

3. Analyses

3.1. Interfacial debond shear strength

A rigorous analytical solution to determine the interfacial debond shear strength (τ_s) was proposed by Hsueh for the two-phase mini-composite with an isotropic fiber embedded in the isotropic matrix shell [5]. The Hsueh model is quite-sophisticated from the viewpoint that it considers the precise interactions at the interface: (1) the radial dependence of the axial stresses in both the fiber and the matrix, (2) the shear stress distribution in the matrix, and (3) the exact equilibrium equation relating the tangential stress to the radial stress at the interface.

The first modification to the Hsueh model is to capture the anisotropy of the fiber core and the matrix. This study assumes that the fiber core with a layered structure is transversely isotropic and each interface in the fiber core, i.e., SCS-9A™/BPyC and BPyC/IPyC, is kept continuous, i.e., a mechanical load can be transferred without any loss at the bonded interface. This should be reasonable because no cracking occurred in the core material unless the BPyC or IPyC failed by shear [3].

The second modification is to consider the effect of the thermally-induced residual stresses on τ_s. Even though there is only a slight mismatch in thermal expansion coefficients between the fiber and the matrix, large thermally-induced residual stresses can be generated during cooling from the processing temperature to the room temperature. Similar to the stress continuity, this study assumes that the interfaces in the fiber core are continuous for thermal conductance.

Fig. 2 shows a schematic illustration of the test system concerned, where the cylindrical polar coordinate system is used and r, θ and z indicate radial, hoop and axial coordinates, respectively. In Fig. 2, a fiber with a radius of a is embedded in the center of a coaxial cylindrical shell of matrix with an outer radius of b and a length of t. The fiber is subjected to an applied stress of σ_0 at one end of the specimen at $z = t$. In this study, the compressive stress is always negative, unless otherwise notified. The stress is transferred from the fiber to the matrix through the interfacial shear stress τ_i. It is worth noting that the anisotropy in elastic constants of the fiber and the matrix is addressed explicitly in the model. The axial and radial Young's moduli of the constituents are represented as E_z and E_r,

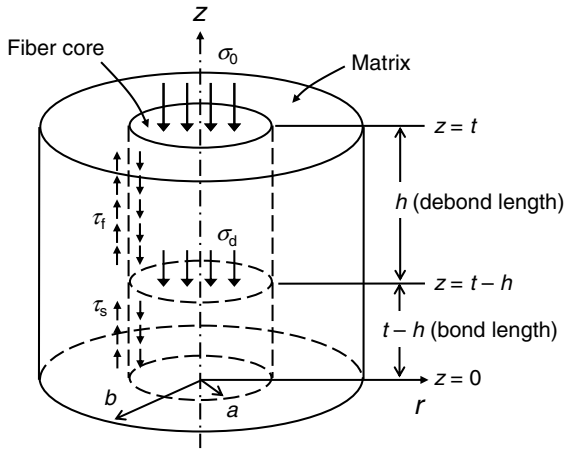

Fig. 2. A schematic illustration of cylindrical polar coordinates.

respectively. Similarly, the axial and radial Poisson's ratios are represented as $\nu_{r\theta}$ and ν_{rz}, respectively. Additionally, the coefficients of thermal expansion in the axial and radial directions are represented as α_z and α_r, respectively.

Assuming radial symmetry, radial, hoop and axial displacements are expressed as $u_r = u(r)$, $u_\theta = 0$ and $u_z = w(r,z)$, respectively. In this case, Hooke's law can be rewritten in the more general form

$$\sigma_{rr} = C_{11}\frac{\partial u(r)}{\partial r} + C_{12}\frac{u(r)}{r} + C_{13}\frac{\partial w(r,z)}{\partial z} - \beta_1 \Delta T, \tag{1}$$

$$\sigma_{\theta\theta} = C_{12}\frac{\partial u(r)}{\partial r} + C_{11}\frac{u(r)}{r} + C_{13}\frac{\partial w(r,z)}{\partial z} - \beta_1 \Delta T, \tag{2}$$

$$\sigma_{zz} = C_{13}\frac{\partial u(r)}{\partial r} + C_{13}\frac{u(r)}{r} + C_{33}\frac{\partial w(r,z)}{\partial z} - \beta_3 \Delta T, \tag{3}$$

$$\tau_{rz} = C_{44}\frac{\partial w(r,z)}{\partial r}, \tag{4}$$

$$\tau_{\theta z} = \tau_{r\theta} = 0, \tag{5}$$

where

$$\beta_1 = (C_{11} + C_{12})\alpha_r + C_{13}\alpha_z, \tag{6}$$

$$\beta_3 = 2C_{13}\alpha_r + C_{33}\alpha_z. \tag{7}$$

Elastic constants of the transversely isotropic material, C_{11}, C_{12}, C_{13}, C_{33} and C_{44}, are given in Appendix A. The temperature range of cooling where the thermal stresses build up is denoted as ΔT. Then, Eqs. (1)–(3) can be further rewritten as

$$\frac{\partial u_r}{\partial r} = \frac{\partial u(r)}{\partial r} = \frac{1}{E_r}\sigma_{rr} - \frac{\nu_{r\theta}}{E_r}\sigma_{\theta\theta} - \frac{\nu_{rz}}{E_z}\sigma_{zz} + \alpha_r \Delta T, \quad (8)$$

$$\frac{\partial u_\theta}{\partial \theta} = \frac{u(r)}{r} = -\frac{\nu_{r\theta}}{E_r}\sigma_{rr} + \frac{1}{E_r}\sigma_{\theta\theta} - \frac{\nu_{rz}}{E_z}\sigma_{zz} + \alpha_r \Delta T, \quad (9)$$

$$\frac{\partial u_z}{\partial z} = \frac{\partial w(r,z)}{\partial z} = -\frac{\nu_{rz}}{E_z}\sigma_{rr} - \frac{\nu_{rz}}{E_z}\sigma_{\theta\theta} + \frac{1}{E_z}\sigma_{zz} + \alpha_z \Delta T. \quad (10)$$

Eqs. (3)–(6) in Ref. [5] are therefore replaced by Eqs. (4) and (8), (9), (10), respectively.

Combining the original Hsueh model, the precise stress interactions at the interface can be expressed. As a guideline of the original Hsueh model [5], Eqs. (17) and (20) in Ref. [5] are finally rewritten as follows:

$$\sigma_{\mathrm{fa}} = \bar{\sigma}_{\mathrm{f}} - \frac{a^2 E_z^{\mathrm{f}}}{8 G_z^{\mathrm{f}}} \frac{\mathrm{d}^2 \bar{\sigma}_{\mathrm{f}}}{\mathrm{d}z^2}, \quad (11)$$

$$a^2 B_1 \frac{\mathrm{d}^2 \bar{\sigma}_{\mathrm{f}}}{\mathrm{d}z^2} = \bar{\sigma}_{\mathrm{f}} - \sigma_0 + \left(\frac{b^2}{a^2} - 1\right)\sigma_{\mathrm{ma}}, \quad (12)$$

where σ_{fa} and σ_{ma} are the axial stresses in the fiber and the matrix at the fiber/matrix interface ($r = a$), respectively, and $\bar{\sigma}_{\mathrm{f}}$ is the average axial stress in the fiber. An axial Young's modulus and a shear modulus of the fiber are denoted as E_z^{f} and G_z^{f}, respectively. A constant B_1 is defined in Appendix B.

For a completely bonded interface, the continuity conditions in both axial and radial directions are required at the interface. We set a radial stress at the interface as σ_i in equilibrium. By profiling the distribution of residual stresses [7,8], the radial and hoop stresses are uniformly distributed in the fiber and both stresses are equal to σ_i. In contrast, the residual stresses in the matrix are expressed as

$$\sigma_{rr}^{\mathrm{m}} = \sigma_i, \quad (13)$$

$$\sigma_{\theta\theta}^{\mathrm{m}} = -\frac{b^2 + a^2}{b^2 - a^2}\sigma_i. \quad (14)$$

From Eqs. (8)–(10), the following continuity conditions are derived:

$$\alpha_r^{\mathrm{f}} \Delta T + \frac{(1 - \nu_{r\theta}^{\mathrm{f}})\sigma_i}{E_r^{\mathrm{f}}} - \frac{\nu_{rz}^{\mathrm{f}} \sigma_{\mathrm{fa}}}{E_z^{\mathrm{f}}} = \alpha_r^{\mathrm{m}} \Delta T - \frac{1}{E_r^{\mathrm{m}}}\left(\frac{b^2 + a^2}{b^2 - a^2} + \nu_{r\theta}^{\mathrm{m}}\right)\sigma_i - \frac{\nu_{rz}^{\mathrm{m}} \sigma_{\mathrm{ma}}}{E_z^{\mathrm{m}}}, \quad (15)$$

$$\alpha_z^{\mathrm{f}} \Delta T + \frac{\sigma_{\mathrm{fa}} - 2\nu_{rz}^{\mathrm{f}}\sigma_i}{E_z^{\mathrm{f}}} = \alpha_z^{\mathrm{m}} \Delta T + \frac{1}{E_z^{\mathrm{m}}}\left(\sigma_{\mathrm{ma}} + \frac{2a^2 \nu_{rz}^{\mathrm{m}}}{b^2 - a^2}\sigma_i\right). \quad (16)$$

where the superscripts of 'f' and 'm' denote the fiber and the matrix, respectively. Using Eqs. (15) and (16), σ_{ma} can be expressed as a function of σ_{fa}.

Adopting the first (Eqs. (11) and (12)) and the second (Eqs. (15) and (16)) modifications, the following differential equation can be obtained

$$a^2 X_1 \frac{\mathrm{d}^2 \bar{\sigma}_{\mathrm{f}}}{\mathrm{d}z^2} + X_2 \bar{\sigma}_{\mathrm{f}} + X_3 + \sigma_0 = 0, \quad (17)$$

where X_1, X_2 and X_3 are constants, defined in Appendix B. A general solution of Eq. (17) has the following form:

$$\bar{\sigma}_{\mathrm{f}} = Y_1 \exp(mz) + Y_2 \exp(-mz) + Y_3, \quad (18)$$

where Y_1, Y_2, Y_3 and m are given in Appendix B, considering the boundary conditions; $\bar{\sigma}_{\mathrm{f}} = 0$ at $z = 0$ and $\bar{\sigma}_{\mathrm{f}} = \sigma_0$ at $z = t$.

Additionally, the following stress equilibrium condition should be satisfied at the interface:

$$\frac{\mathrm{d}\bar{\sigma}_{\mathrm{f}}}{\mathrm{d}z} = -\frac{2\tau_i}{a}. \quad (19)$$

Combining Eqs. (18) and (19), the interfacial shear stress at the fiber/matrix interface can be expressed as a function of z. The interfacial shear stress is maximized at $z = t$, yielding τ_{s}. When the debonding initiates ($z = t$), σ_0 is replaced by the debond initiation stress (σ_{d}). The resultant equation is

$$\tau_{\mathrm{s}} = -\left(\frac{am}{2}\right)\frac{[\exp(mt) + \exp(-mt)]\sigma_{\mathrm{d}} + \frac{\sigma_{\mathrm{d}} + X_3}{X_2}[\exp(mt) + \exp(-mt) - 2]}{\exp(mt) - \exp(-mt)}. \quad (20)$$

3.2. Interfacial friction stress

After initial debonding, frictional sliding occurs at the debonded interface. The interfacial friction stress (τ_{f}) is therefore recognized as a good measure to represent interfacial shear properties for the partially ($0 < h < t$) or completely ($h = t$) debonded interface, where the debond length is denoted as h. In the previous paper by the authors [3], Shetty's non-linear shear-lag model [6] was employed to predict the interfacial friction stress for a completely debonded interface from the data of $\sigma_{\max}$. The major advantage to use this model is that the analysis is independent of the shape of the indentation curve, i.e., it is applicable to composites with strong interfacial bonds. Similar to the evaluation of interfacial debond shear strength, this study provides a more precise solution using Hooke's Law for the transversely isotropic system.

At the debonded interface, the applied stress is transferred primarily by Coulomb friction. The interfacial friction stress is then expressed as

$$\tau_f = -\mu(\sigma_c + \sigma_p), \tag{21}$$

where μ is the coefficient of friction, σ_c is the combination of radial stresses induced at the debonded interface by the thermal expansion mismatch and the fiber surface roughness, and σ_p is the radial stress due to Poisson's expansion of the fiber. Thermal residual stresses are, in general, tensile stresses for the TRISO-coated tube, then, beyond debonding, there would be a less interaction between the fiber core and the SiC layer. For simplicity, this study assumes that, for debonded interface, the axial stresses in the fiber and the matrix are independent of the radial coordinate, i.e., the axial stress in the fiber core is defined as an average axial stress, $\bar{\sigma}_f$. However, the rough surface induces very high compressive clamping stress at the debonded interface as discussed later. Therefore, in actuality, there remains the stress interaction between the fiber core and the SiC layer, generating the axial stresses dependent on the radial coordinate. Such a complicated stress interaction makes it very difficult to solve interfacial friction issue at the debonded interface. Then, the Poisson's expansion-induced radial stress can be simplified as [9]

$$\sigma_p = \left[\frac{\nu_{rz}^f}{E_z^f} + \frac{a^2\nu_{rz}^m}{(b^2-a^2)E_z^m}\right]B_2\bar{\sigma}_f - \frac{a^2\nu_{rz}^m B_2\sigma_0}{(b^2-a^2)E_z^m}. \tag{22}$$

Then Eq. (21) can be rewritten as

$$\tau_f = -\mu(\sigma_c + k_1\bar{\sigma}_f + k_2\sigma_0), \tag{23}$$

where

$$k_1 = \left[\frac{\nu_{rz}^f}{E_z^f} + \frac{a^2\nu_{rz}^m}{(b^2-a^2)E_z^m}\right]B_2, \tag{24}$$

$$k_2 = -\frac{a^2\nu_{rz}^m B_2}{(b^2-a^2)E_z^m}. \tag{25}$$

Substituting Eq. (23) into Eq. (19), integrating, and applying the boundary condition $\bar{\sigma}_f = \sigma_0$ at $z = t$, gives the following solution for the axial stress in the fiber:

$$\bar{\sigma}_f = \left(\frac{k_1+k_2}{k_1}\sigma_0 + \frac{\sigma_c}{k_1}\right)\exp\left[\frac{2\mu k_1(z-t)}{a}\right] - \frac{k_2\sigma_0+\sigma_c}{k_1}. \tag{26}$$

For a given applied stress σ_0, there is a finite fiber debonded length (h^*) at which the axial stress reduces to σ_d.

$$h^* = \frac{a}{2\mu k_1}\ln\left[\frac{(k_1+k_2)\sigma_0+\sigma_c}{k_1\sigma_d + k_2\sigma_0 + \sigma_c}\right]. \tag{27}$$

At complete sliding ($h^* = t$), the stress applied to push-out the fiber reaches a maximum. In contrast, σ_d becomes zero as the bonded length approaches zero. Consequently, the complete sliding stress (σ_{max}) can be obtained by

$$\sigma_{max} = \frac{\sigma_c\left[\exp\left(\frac{2\mu k_1 t}{a}\right) - 1\right]}{k_1 - k_2\left[\exp\left(\frac{2\mu k_1 t}{a}\right) - 1\right]}. \tag{28}$$

In contrast, the intrinsic interfacial friction stress (τ_f^{int}) is determined by the product of μ and σ_c, the latter of which is induced by the thermal expansion mismatch (σ_{th}) and the fiber surface roughness (σ_{rough})

$$\tau_f^{int} = -\mu\sigma_c = -\mu(\sigma_{th} + \sigma_{rough}), \tag{29}$$

where

$$\sigma_{th} = B_2(\alpha_r^m - \alpha_r^f)\Delta T, \tag{30}$$

$$\sigma_{rough} = -\frac{AB_2}{a}, \tag{31}$$

In Eq. (31), A is the average fiber surface roughness. During the fiber sliding, the average strain of A/a is induced at the interface, producing a radial clamping stress at the interface.

On the other hand, the average interfacial friction stress ($\bar{\tau}_f$) can be estimated from the plateau stress ($\sigma_{plateau}$) after the complete sliding [10]

$$\bar{\tau}_f = -\frac{\sigma_{plateau}a}{2t}. \tag{32}$$

For very thin specimens, Eq. (28) is expressed as the same form with Eq. (32).

3.3. Material parameters used in analyses

Material properties used in analysis are summarized in Table 1. In the table, CVD SiC, BPyC and IPyC are considered to be isotropic. Of the extensive database on CVD SiC, data contained in the product sheet from Rohm and Haas Company Advanced Materials (Waborn, MA, USA) is considered the most reliable and applicable. A coefficient of thermal expansion of 4.0×10^{-6}/K over the temperature range from 298–1273 K for Rohm & Haas CVD SiC is slightly lower than that of other CVD materials reported in literature. Recently required data suggests using a value of 4.4×10^{-6}/K (298–1273 K) for CVD SiC [11–14]. Fundamental data of PyC are quoted from the CEGA handbook

Table 1
Material properties used in analyses

	d (g/cm^3)	E_z (GPa)	E_r (GPa)	$\nu_{r\theta}$	ν_{rz}	G_z (GPa)[a]	α_z (10^{-6}/K)[b]	α_r (10^{-6}/K)[b]
SCS-9A SiC fiber[c]	2.8	307	200	0.2	0.3	128	4.3	4.3
Buffer isotropic PyC[d]	~1	20	20	0.23	0.23	8	5.5	5.5
Inner isotropic PyC[d]	~2	30	30	0.23	0.23	12	5.5	5.5
CVD SiC[e]	3.21	460	460	0.21	0.21	190	4.4[f]	4.4[f]
Fiber core[a]	1.65	64	30	0.23	0.27	12	4.7	5.4

[a] Calculated by Hashin's theory [16].
[b] Average over the temperature range 298–1273 K.
[c] Product sheet form Specialty Materials, Inc. (Transverse properties are calculated by Hashin's theory [16]).
[d] Estimated from CEGA report [15].
[e] Product sheet from Rohm and Haas Co.
[f] Thermal expansion coeffieient data from recent review [11–14].

[15]. It is noted that an improved data set for PyC is warranted.

The SCS-9A™ SiC fiber composed of a carbon core surrounded by SiC is transversely isotropic. From the manufacturer's product sheet, the elastic and thermal properties in the fiber longitudinal direction are provided. However, the material properties in the radial direction are unknown. In this study, the radial properties are estimated by Hashin's theory [16], which has been developed to predict elastic and thermal properties for a transversely isotropic material. Assuming that the SCS-9A™ fiber consists of dense and pure SiC with a high-density isotropic carbon core and volume fraction of ~0.20, a transverse Young's modulus of 200 GPa and a transverse Poisson's ratio of 0.3 are roughly estimated. The minor difference in the thermal expansion coefficient is estimated.

Similarly, the elastic constants and thermal expansion coefficient are calculated for the punched-out inner core using Hashin's transversely isotropic model and they are listed in Table 1.

4. Results and discussion

4.1. Thermal expansion mismatch-induced residual stresses

Fig. 3 shows the calculated distribution of thermal residual stresses in a model TRISO-coated tube, generated using conventional thermal stress models [9,10]. Thermal residual stresses are evaluated by the two-phase model, considering the fiber core (SCS-9A™ + BPyC + IPyC) with a SiC coating, and the four-phase multilayer model, considering the individual four layers separately. The results show that the thermal expansion mismatch gives small residual tensile stresses at the interface for the tube specimen (~50 MPa). In Fig. 3, there are some stress gaps at the IPyC/SiC interface between these two different analytical results but they are negligibly small. The slight difference in the two models should not have a significant influence on the test results, i.e., the assumption that the core material properties can be averaged by the rule of mixtures seems reasonable for the tube material.

Fig. 3 also shows the stress distributions of a TRISO-coated particle. Note that thicknesses of each layer are identical to the model TRISO-coated tube. It is apparent that the results of the two-phase model analysis for the particle show substantially higher residual tensile stresses in both radial and hoop directions. In contrast, for four-phase model analysis, both radial and hoop residual stresses of the particle are in good agreement with those of the cylindrical material. Thus it is concluded that averaging material properties of the constituents in the core is inappropriate for the particle case.

4.2. Interfacial debond shear strength

Fig. 4 plots the ratio of the interfacial debond shear strength to the debond initiation stress ($-\tau_s/\sigma_d$) as a function of specimen thickness. In Fig. 4, the existing isotropic model and the transversely isotropic model proposed in this study are compared. Additionally the effect of thermal expansion mismatch is presented. For the very thin specimens ($t < 30$ μm), there is no significant difference among the models. However, for thick specimens ($t > 30$ μm), the results obtained by the isotropic model show 50% higher $-\tau_s/\sigma_d$ ratio than obtained by the transversely isotropic model. Unless the thermal effect is considered, the ratio would be underestimated. These facts suggest that the solution of

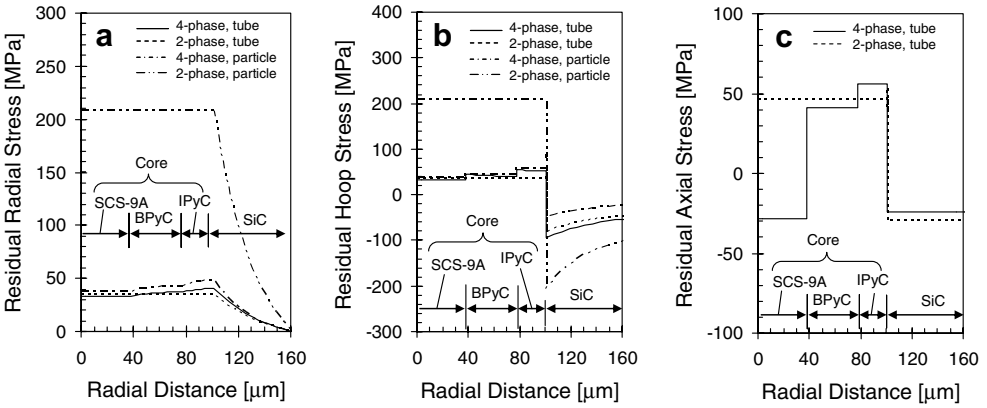

Fig. 3. Calculated thermal residual stresses for a model TRISO-coated tube and a particle: (a) radial, (b) hoop and (c) axial.

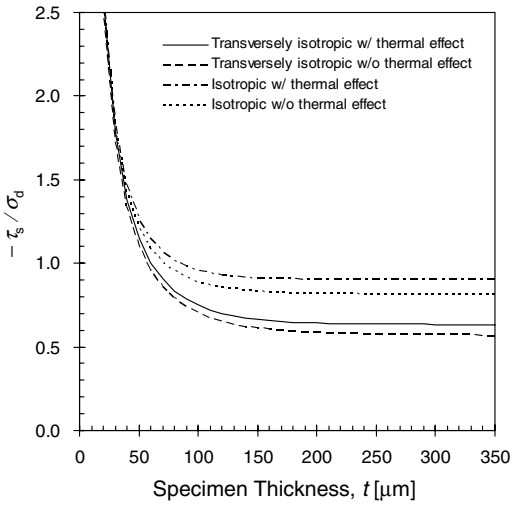

Fig. 4. Comparison of the interfacial debond shear strengths between the isotropic and transversely isotropic models.

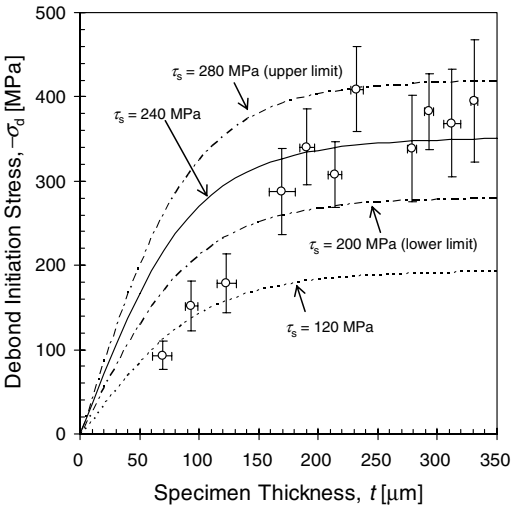

Fig. 5. Interfacial debond initiation stress (σ_d) of a model TRISO-coated tube. The curves fitted by Eq. (20) are also plotted as a function of specimen thickness, providing interfacial debond shear strengths (τ_s).

Eq. (20) can give a reliable value for τ_s, while the other models may bias the results.

According to the preliminary work by the authors [3], it was confirmed that the data on the debond initiation stress (σ_d) are valid for all specimens in a thickness range from $t = 60$ to 340 μm. The debond initiation stress monotonically increases with increasing specimen thickness and approaches a constant when $t > 160$ μm (Fig. 5). By fitting Eq. (20) to the experimental data of σ_d for $t > 160$ μm, an interfacial debond shear strength (τ_s) of 240 ± 40 MPa was obtained. As discussed previously [3], for thin specimens ($t < 120$ μm), the value of τ_s becomes lower than the values expected from Eq. (20). It is believed to be due primarily to the effect of the stress relief from the open edge at the interface. For this reason, analysis of push-out for thicknesses less than 120 μm specimens might result in incorrectly low values. Compared with the value of τ_s obtained by the original isotropic model (~280 MPa), the value of τ_s in this study (240 MPa) appears low. However, this stress level is still quite high as the crack primarily propagated within the transient phase between IPyC and SiC [3]. This high τ_s enables significant loads to be transferred at the IPyC/SiC interface. The large scatter of the data is attributed to the probabilistic nature of debond initiation stress. According to the sensitivity analysis of the parameters, the effects of measurement errors from the specimen size and the elastic constants are seemingly very small. For instance, 10% scatter of elastic modulus provides less than 5% scatter in the results. Similarly

10% scatter of thermal expansion coefficient gives at most 1% data scatter.

The interfacial debond shear strength of a TRISO-coated particle can be estimated considering the semi-infinite specimen thickness case. Because of no significant difference obtained in the magnitude of thermal residual stresses between the cylindrical specimen and the spherical specimen (Fig. 3), it is speculated that the value of τ_s for the TRISO-coated particle would be in the same order with that of the tube specimen (~240 MPa).

4.3. Interfacial friction stress

The model TRISO-coated tube of this failed by shear deformation of the inner core material when the specimen thickness was greater than 230 μm. This is because the applied stress overcomes the shear strength of PyC before reaching the complete sliding stress at the interface. In such a situation, complete sliding never occurred. The modified Shetty's model was therefore applied to the data of the thin specimens ($t < 230$ μm) coupled with the graceful fracture at the IPyC/SiC interface.

Fig. 6 shows the complete sliding stress as a function of specimen thickness, where the fitting curves derived from Eqs. (28) and (32) are also plotted. Modified Shetty's model for a transversely isotropic material gives the friction coefficient of 0.35 and the residual radial stress of −350 MPa, yielding an intrinsic interfacial friction stress of 123 MPa. Similarly the upper and lower limits were obtained, giving data scatter of ~40 MPa. The friction coefficient in this work is slightly higher than that determined in the previous study [3] for the material assumed to be isotropic (~0.23), while there is no significant difference in the residual radial stress (−350 MPa). This indicates that the original Shetty's model for the isotropic material therefore underestimates the interfacial friction stress (cf. 80 MPa in Ref. [3]). Of particular emphasis is that the intrinsic interfacial friction stress by Eqs. (28) and (29) is identical to the average interfacial friction stress estimated by the plateau stress (~120 MPa). The plateau stress approach as an alternate method to predict the interfacial friction stress, then, is useful and much easier to apply.

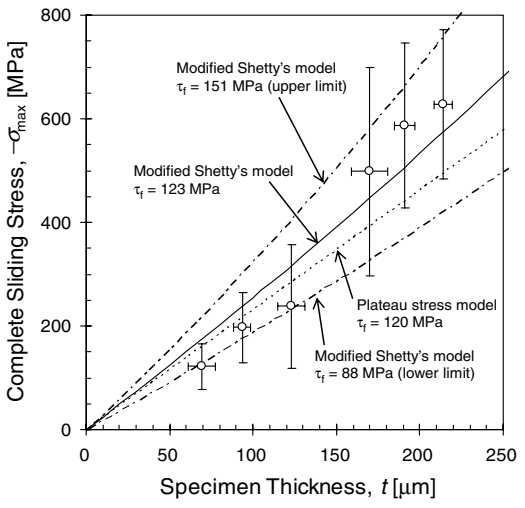

Fig. 6. Complete sliding stress (σ_{max}) of a model TRISO-coated tube. The curves fitted by Eq. (28) are plotted as a function of specimen thickness, providing interfacial friction stresses (τ_f). The result by the plateau stress model (Eq. (32)) is also presented in the figure.

The high residual radial stress (−350 MPa) may impose a high residual hoop stress on the SiC coating. According to the stress analysis, the residual hoop stress of ~500 MPa is anticipated in the SiC coating. On the other hand, the hoop strength of SiC, which was measured by the internal pressurization technique for thin-walled miniature tube specimens, is 310–450 MPa [17]. Considering the effect of specimen size [18], the hoop strength of the SiC layer of the model TRISO-coated tube is more than 580 MPa. Therefore, the failure of a SiC layer by internal pressurization seems unlikely.

From Fig. 3, it is apparent that the thermal expansion mismatch between the fiber core and the SiC coating is not significant and, similar to the interfacial debond shear strength evaluation,

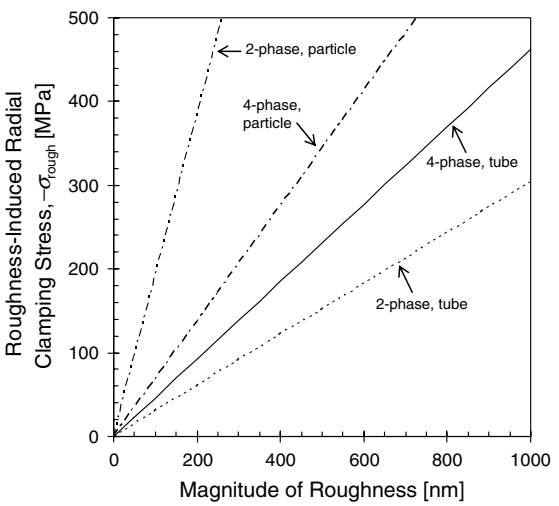

Fig. 7. Calculated roughness-induced radial stresses at the interface.

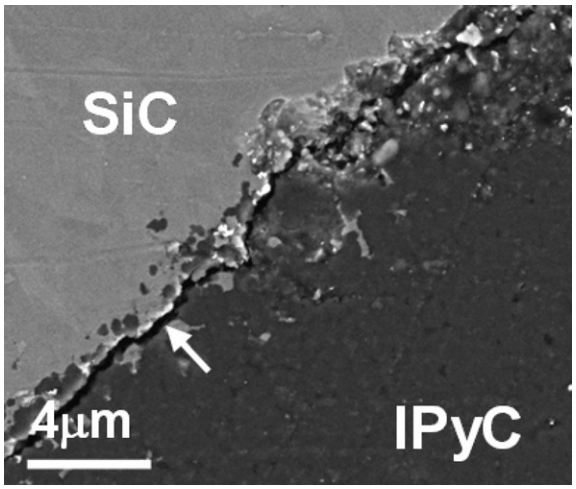

Fig. 8. A typical micrograph depicting crack propagation at the IPyC/SiC interface.

the slight mismatch in the thermal expansivity therefore has a minor effect on the interfacial friction stress. Contrarily, the significant residual radial stress at the interface is due primarily to the roughness at the crack surface. In Fig. 7, the calculated roughness-induced radial stress is presented as a function of the magnitude of roughness. The prediction from the four-phase composite model is also plotted in the figure. The figure shows that Eq. (31) for the two-phase model gives a lower clamping stress. Taking a more realistic value from the four-phase composite model, the roughness at the interface can be estimated to be ~800 nm. According to the micrograph of the crack propagation at the IPyC/SiC interface (Fig. 8), this might be a good approximation. Originally, the tortuous IPyC/SiC interface formed by CVD does not allow the crack propagation along the actual boundary between IPyC and SiC, giving a very rough crack plane. Similarly, the large friction coefficient would be attributed to the rough surface at the interface.

In Fig. 7, the roughness-induced clamping stress for the TRISO-particle is quite higher than that for the tube specimen. The significantly high roughness-induced stress may increase interfacial friction (>120 MPa), resulting in very strong interface even for the debonded case. The strong interface may allow crack propagation at the interface, eventually causing a failure of the outer SiC coating.

5. Conclusions

In order to evaluate the shear properties at the IPyC/SiC interface of the transversely isotropic TRISO-coating, the existing non-linear shear-lag models for the interfacial debond shear strength and the interfacial friction stress were rearranged and the interfacial shear data previously reported were properly reanalyzed in this study. Major conclusions are summarized as follows:

1. The non-linear shear-lag model for a transversely isotropic material system gives rigorous solutions in determining (1) the interfacial debond shear strength and (2) the interfacial friction stress of the TRISO-coating. This model also considers the effects of residual stresses induced by the thermal expansion mismatch between each coating layer and the fiber surface roughness.
2. The existing isotropic model overestimates the interfacial debond shear strength. The more reliable value of 240 ± 40 MPa was obtained by the refined transversely isotropic model. Such a high interfacial strength could allow significant loads to be transferred at the IPyC/SiC interface.
3. The original Shetty's isotropic model contrarily underestimates the interfacial friction stress. This study gives an intrinsic interfacial friction stress of 120 ± 30 MPa with a friction coefficient of ~0.35 and a radial clamping (compressive) stress of ~350 MPa. The considerably high friction stress is attributed primarily to the roughness at the cracked interface rather than the thermal effect.

Acknowledgements

The authors would like to thank Drs Edgar Lara-Curzio and Song-Gu Hong for reviewing the manuscript. This research was sponsored by the US Department of Energy Office of Nuclear Energy, Science and Technology, a Nuclear Energy Research Initiative (NERI) Project, under contract NEAF355 (AF3510) with Oak Ridge National Laboratory (operated by UT-Battelle, LLC).

Appendix A

The engineering elastic constants for a transversely isotropic material are expressed as follows:

$$C_{11} = \frac{E_r}{E_z}\left(\frac{E_z - E_r v_{rz}^2}{D}\right), \tag{A1}$$

$$C_{12} = \frac{E_r}{E_z}\left(\frac{E_z v_{r\theta} + E_r v_{rz}^2}{D}\right), \tag{A2}$$

$$C_{13} = E_z \frac{v_{rz}(1+v_{r\theta})}{D}, \tag{A3}$$

$$C_{33} = E_z \frac{1-v_{r\theta}^2}{D}, \tag{A4}$$

$$C_{44} = G_z, \tag{A5}$$

where

$$D = \left(1 - \frac{v_{rz}^2 E_r}{E_z}\right)^2 - \left(v_{r\theta} + \frac{v_{rz}^2 E_r}{E_z}\right)^2. \tag{A6}$$

Appendix B

The coefficients in Eqs. (17) and (18) are given by

$$X_1 = B_1 + \frac{(b^2-a^2)E_z^{\mathrm{f}} B_5}{8a^2 G_z^{\mathrm{f}} B_4}, \tag{B1}$$

$$X_2 = -\left[1 + \frac{(b^2-a^2)B_5}{a^2 B_4}\right], \tag{B2}$$

$$X_3 = -\frac{(b^2-a^2)}{a^2 B_4}\left[B_2(\alpha_r^{\mathrm{m}} - \alpha_r^{\mathrm{f}}) - B_3(\alpha_z^{\mathrm{m}} - \alpha_z^{\mathrm{f}})\right]\Delta T, \tag{B3}$$

$$Y_1 = \frac{\sigma_0 - Y_3[1-\exp(-mt)]}{\exp(mt) - \exp(-mt)}, \tag{B4}$$

$$Y_2 = -\frac{\sigma_0 - Y_3[1-\exp(mt)]}{\exp(mt) - \exp(-mt)}, \tag{B5}$$

$$Y_3 = -\frac{\sigma_0 + X_3}{X_2}, \tag{B6}$$

$$m = \frac{1}{a}\sqrt{-\frac{X_2}{X_1}}, \tag{B7}$$

where

$$B_1 = \frac{E_z^{\mathrm{m}} b^2}{2G_z^{\mathrm{m}}(b^2-a^2)}\left[\frac{b^2}{a^2}\ln\left(\frac{b}{a}\right) - \frac{(b^2-a^2)(3b^2-a^2)}{4a^2b^2}\right], \tag{B8}$$

$$B_2 = \frac{1}{\frac{1-v_{r\theta}^{\mathrm{f}}}{E_r^{\mathrm{f}}} + \frac{1}{E_r^{\mathrm{m}}}\left(\frac{b^2+a^2}{b^2-a^2} + v_{r\theta}^{\mathrm{m}}\right)}, \tag{B9}$$

$$B_3 = -\frac{1}{\frac{2v_{rz}^{\mathrm{f}}}{E_z^{\mathrm{f}}} + \frac{2a^2 v_{rz}^{\mathrm{m}}}{E_z^{\mathrm{m}}(b^2-a^2)}}, \tag{B10}$$

$$B_4 = \frac{B_2 v_{rz}^{\mathrm{m}} + B_3}{E_z^{\mathrm{m}}}, \tag{B11}$$

$$B_5 = \frac{B_2 v_{rz}^{\mathrm{f}} + B_3}{E_z^{\mathrm{f}}}. \tag{B12}$$

References

[1] A technology roadmap for Generation IV nuclear energy systems, US DOE Nuclear Energy Research Advisory Committee and the Generation IV International Forum, 2002.

[2] D.A. Petti, J. Buongiorno, J.T. Maki, R.R. Hobbins, G.K. Miller, Nucl. Eng. Des. 222 (2003) 281.

[3] T. Nozawa, L.L. Snead, Y. Katoh, J.H. Miller, E. Lara-Curzio, J. Nucl. Mater. 350 (2006) 182.

[4] E. Lara-Curzio, M.K. Ferber, J. Mater. Sci. 29 (1994) 6152.

[5] C.-H. Hsueh, Mater. Sci. Eng. A154 (1992) 125.

[6] D.K. Shetty, J. Am. Ceram. Soc. 71 (1988) C107.

[7] Y. Mikata, M. Taya, J. Compos. Mater. 19 (1985) 554.

[8] H.J. Oel, V.D. Frechette, J. Am. Ceram. Soc. 69 (1986) 342.

[9] C.-H. Hsueh, Mater. Sci. Eng. A161 (1993) L1.

[10] F. Rebillat, J. Lamon, R. Naslain, E. Lara-Curzio, M.K. Ferber, T.M. Besmann, J. Am. Ceram. Soc. 81 (1998) 965.

[11] M.A. Pickering, R.L. Taylor, J.T. Keeley, G.A. Graves, Nucl. Instrum. and Meth. A 291 (1990) 95.

[12] Z. Li, R.C. Bradt, J. Mater. Sci. 21 (1986) 4366.

[13] H. Suzuki, T. Iseki, M. Ito, J. Nucl. Mater. 48 (1973) 247.

[14] A.F. Pojur, B. Yates, B.T. Kelly, J. Phys. D 5 (1972) 1321.

[15] CEGA, Report CEGA-002820, Rev 1 (July 1993).

[16] Z. Hashin, J. Appl. Mech. 46 (1979) 543.

[17] T.-S. Byun, S.-G. Hong, L.L. Snead, Y. Katoh, Miniaturized fracture stress tests for thin-walled tubular SiC specimens, in: 30th Annual International Conference on Advanced Ceramics & Composites, Cocoa Beach, FL, USA, 2005.

[18] S.-G. Hong, T.-S. Byun, R.A. Lowden, L.L. Snead, Y. Katoh, J. Am. Ceram. Soc. 90 (2007) 184.